How to cite: *Angew. Chem. Int. Ed.* **2024**, *63*, e202402841
doi.org/10.1002/anie.202402841

Ammonia Production

Controlled Synthesis of Unconventional Phase Alloy Nanobranches for Highly Selective Electrocatalytic Nitrite Reduction to Ammonia

Yunhao Wang[+], Yuecheng Xiong[+], Mingzi Sun[+], Jingwen Zhou[+], Fengkun Hao, Qinghua Zhang, Chenliang Ye, Xixi Wang, Zhihang Xu, Qingbo Wa, Fu Liu, Xiang Meng, Juan Wang, Pengyi Lu, Yangbo Ma, Jinwen Yin, Ye Zhu, Shengqi Chu, Bolong Huang, Lin Gu,* and Zhanxi Fan**

Abstract: The controlled synthesis of metal nanomaterials with unconventional phases is of significant importance to develop high-performance catalysts for various applications. However, it remains challenging to modulate the atomic arrangements of metal nanomaterials, especially the alloy nanostructures that involve different metals with distinct redox potentials. Here we report the general one-pot synthesis of IrNi, IrRhNi and IrFeNi alloy nanobranches with unconventional hexagonal close-packed (hcp) phase. Notably, the as-synthesized hcp IrNi nanobranches demonstrate excellent catalytic performance towards electrochemical nitrite reduction reaction (NO_2RR), with superior NH_3 Faradaic efficiency and yield rate of 98.2 % and 34.6 $mg\,h^{-1}\,mg_{cat}^{-1}$ (75.5 $mg\,h^{-1}\,mg_{Ir}^{-1}$) at 0 and −0.1 V (vs reversible hydrogen electrode), respectively. Ex/in situ characterizations and theoretical calculations reveal that the Ir–Ni interactions within hcp IrNi alloy improve electron transfer to benefit both nitrite activation and active hydrogen generation, leading to a stronger reaction trend of NO_2RR by greatly reducing energy barriers of rate-determining step.

Introduction

The balance of nitrogen cycle on Earth holds substantial significance for the sustainable development of global ecosystem. However, in the past century, human activities including over-fertilization and fossil fuel combustion have drastically perturbed the equilibrium of the nitrogen cycle, posing severe threats to the health of human and environment.[1–4] In particular, as an essential intermediate in the global nitrogen cycle, nitrite (NO_2^-) is classified as a Group 2A carcinogen by World Health Organization,[5] which can cause critical diseases, such as blue baby syndrome, cellular degradation, and hypertension.[6–8] Therefore, it is imperative to convert hazardous NO_2^- into harmless and useful products to harmonize the nitrogen cycle and sustain the global ecosystem. Among diverse

[*] Y. Wang,[+] Y. Xiong,[+] J. Zhou,[+] F. Hao, X. Wang, Q. Wa, F. Liu, X. Meng, J. Wang, P. Lu, Y. Ma, J. Yin, Prof. Z. Fan
Department of Chemistry, City University of Hong Kong, Kowloon, Hong Kong 999077, China
E-mail: zhanxi.fan@cityu.edu.hk

Y. Xiong,[+] J. Zhou,[+] P. Lu, Prof. Z. Fan
Hong Kong Branch of National Precious Metals Material Engineering Research Center (NPMM), City University of Hong Kong, Kowloon, Hong Kong 999077, China

M. Sun,[+] Prof. B. Huang
Department of Applied Biology and Chemical Technology, The Hong Kong Polytechnic University, Kowloon, Hong Kong 999077, China
E-mail: bhuang@polyu.edu.hk

Prof. Q. Zhang
Institute of Physics, Beijing National Laboratory for Condensed Matter Physics, Chinese Academy of Sciences, Beijing 100190, China

Prof. C. Ye
Department of Power Engineering, North China Electric Power University, Baoding 071003, China

Z. Xu, Prof. Y. Zhu
Department of Applied Physics, Research Institute for Smart Energy, The Hong Kong Polytechnic University, Kowloon, Hong Kong 999077, China

Prof. S. Chu
Beijing Synchrotron Radiation Facility, Institute of High Energy Physics, Chinese Academy of Sciences, Beijing 100049, China

Prof. L. Gu
Beijing National Center for Electron Microscopy and Laboratory of Advanced Materials, Department of Materials Science and Engineering, Tsinghua University, Beijing 100084, China
E-mail: lingu@tsinghua.edu.cn

Prof. Z. Fan
City University of Hong Kong Shenzhen Research Institute, Shenzhen 518057, China

[+] These authors contributed equally to this work.

methods, electrocatalytic NO_2^- reduction reaction (NO_2RR) to ammonia (NH_3) offers a feasible and prospective strategy to address this issue.[9–12] Importantly, NO_2RR can enable the simultaneous removal of NO_2^- contaminant and production of valuable NH_3, which has been widely recognized as carbon-free fuel, green energy carrier and essential chemical feedstock.[13–17] But it should be mentioned that electrocatalytic NO_2RR to NH_3 is a complicated proton-coupled electron transfer process that involves the adsorption/desorption of multiple intermediates, which still suffers from low activity and poor selectivity.[18] So far, tremendous efforts have been devoted to modulating the size,[19–20] composition,[21–23] defect[24–25] and dimension[25–28] of catalysts to improve their performance towards NO_2RR, but the effect of crystal phase, as a key structural parameter, is rarely investigated.

Recently, crystal phase engineering has been emerging as an effective approach to modulate the intrinsic physicochemical properties of metal nanomaterials, and thus improve their catalytic activities.[29–38] To date, various monometallic nanomaterials with unconventional crystal phases, such as face-centered cubic (fcc)-2H-fcc heterophase gold,[39] fcc ruthenium,[40–41] 2H palladium[42] and hexagonal close-packed (hcp) rhodium,[43] have been obtained and demonstrated much superior catalytic activities over their common phase counterparts in different electrochemical reactions. Note that the catalytic performance of monometallic nanomaterials usually suffers from the limited types of adsorption sites on the surface, which makes it difficult to achieve the concurrent adsorption and stabilization of multiple intermediates in the multistep reactions like NO_2RR.[44–45] In this regard, the rational design and delicate construction of unconventional phase alloy nanomaterials composed of different metal elements could be a promising way to optimize their intrinsic properties and further boost their catalytic performance toward NO_2RR. Unfortunately, due to the vast differences in redox potentials, surface energies, and nucleation/growth behaviours of different metal components,[46–49] it remains a big challenge to achieve the controlled synthesis of alloy nanomaterials with unconventional phases.

In this work, we report a facile one-pot solvothermal method for the general synthesis of IrNi, IrRhNi and IrFeNi alloy nanobranches (NBs) with an unconventional hcp phase. The obtained hcp IrNi alloy NBs are composed of a Ni-rich core and an Ir-rich shell. Impressively, hcp IrNi NBs demonstrate outstanding catalytic performance for NO_2RR, with superior Faradaic efficiency (FE) and yield rate of 98.2 % and 34.6 $mg\,h^{-1}\,mg_{cat}^{-1}$ (75.5 $mg\,h^{-1}\,mg_{Ir}^{-1}$) toward NH_3 synthesis at 0 and −0.1 V (vs reversible hydrogen electrode (RHE)), respectively. Furthermore, the consecutive cycling electrolysis measurement suggests the excellent catalytic durability of hcp IrNi NBs. Electron paramagnetic resonance (EPR) and in situ differential electrochemical mass spectrometry (DEMS) results indicate that hcp IrNi NBs can supply abundant active hydrogen for the hydrogenation step and significantly reduce the overpotential for NH_3 production. Density functional theory (DFT) calculations have revealed stronger Ir–Ni interactions in the hcp IrNi alloy than fcc counterpart, which optimizes the electronic structures of both Ni and Ir to supply more efficient electron transfer during NO_2RR. The hcp IrNi alloy generates active hydrogen more efficiently on the surface, which reduces the energy barriers and guarantees superior NO_2RR performance.

Results and Discussion

Synthesis and Structural Characterization

The unconventional hcp phase IrNi alloy NBs were synthesized by a facile one-pot solvothermal method, in which $Ir(acac)_3$ and $Ni(acac)_2$ were co-reduced in the mixture of oleylamine and oleic acid at 220 °C (see Supporting Information for details). The low-magnification transmission electron microscopy (TEM) images show the high purity of the as-prepared hcp IrNi NBs (Figure S1a,b). TEM and high-angle annular dark-field scanning TEM (HAADF-STEM) images demonstrate that the obtained products are composed of multi-rod-like nanobranches (Figure 1a–c). The average length and middle-width of individual nanobranches are 125.6 ± 4.4 nm and 16.6 ± 0.3 nm (Figure S2), respectively. The unconventional hcp phase was identified by the characteristic diffraction rings in the selected-area electron diffraction (SAED) pattern of IrNi NBs (Figure S1c). Meanwhile, the hcp phase was further confirmed by the powder X-ray diffraction (XRD) pattern (Figure S3).

As shown in the spherical aberration-corrected HAADF-STEM images, there is a strong contrast between the inside and outside areas of nanobranches, indicating the unique core-shell structure of hcp IrNi NBs (Figure 1d, e). The crystal structures were characterized by the atomic resolution HAADF-STEM image. As shown in Figure 1e, the zoom-in HAADF-STEM image clearly identify the characteristic stacking sequence of "AB" along the close-packed $[001]_h$ direction of hcp phase (Figure S4). The interplanar spacings of 2.17 (2.20) and 2.21 (2.25) Å are assigned to $(002)_h$ and $(010)_h$ facets of hcp IrNi NBs at the core (shell) sites, respectively. The unconventional hcp phase was further confirmed by the corresponding fast Fourier transform (FFT) pattern of hcp phase along the $[110]_h$ zone axis (Figure 1f). The energy dispersion X-ray spectroscopy (EDS) result shows that the atomic ratio of Ir/Ni is 20.5/79.5 (Figure S5). The EDS line scanning and elemental mapping investigations unravel the alloy structure of hcp IrNi NBs with a Ni-rich core and Ir-rich shell (Figure S6 and Figure 1g–j), which is well consistent with the observation that the lattice spacing at the shell region is larger than that at the core area.

It is worth mentioning that the unconventional hcp phase IrNi NBs can still be obtained by replacing $Ir(acac)_3$ with $IrCl_3{\cdot}xH_2O$. The TEM image shows that the products are composed of multi-rod-like nanobranches (Figure S7a). Its unconventional hcp phase was confirmed by the characteristic diffraction rings in the SAED pattern, which is further identified by the XRD results (Figure S7b, c). The FFT pattern and the characteristic stacking sequence of "AB"

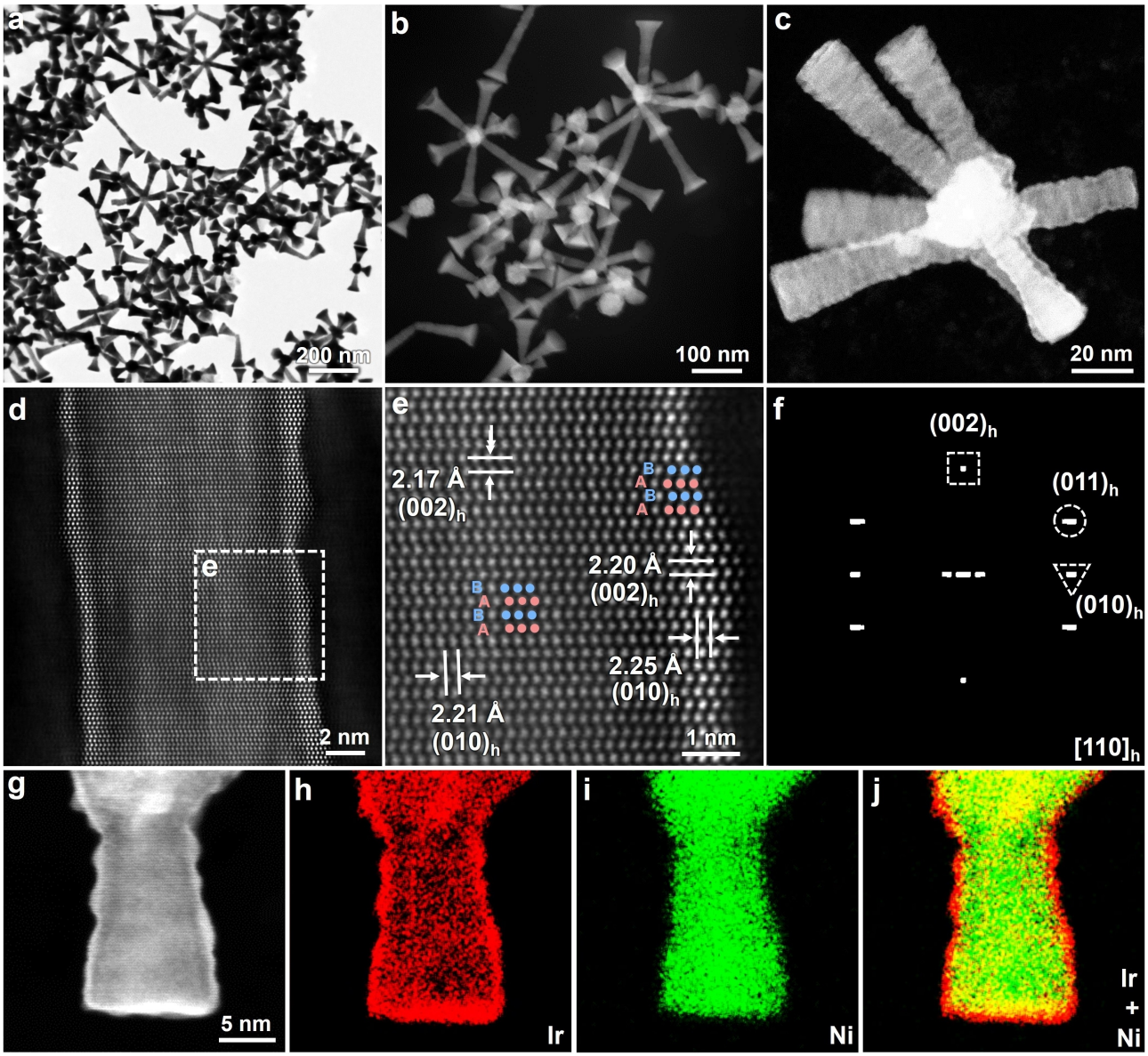

Figure 1. Structural characterization of unconventional hcp phase IrNi alloy NBs. (a, b) TEM (a) and STEM (b) images of hcp IrNi NBs. (c, d) HAADF-STEM (c) and the atomic-resolution HAADF-STEM images (d) of a typical hcp IrNi NB. (e) The zoom-in atomic-resolution HAADF-STEM image from the white dashed square-marked area in (d). (f) The corresponding FFT pattern of the atomic-resolution HAADF-STEM image shown in (d). (g–j) HAADF-STEM image (g) and the corresponding EDS elemental mappings (h–j) of hcp IrNi NBs.

further verify the hcp structure (Figure S7d, e). The Ir/Ni atomic ratio was determined to be 17.4/82.6 (Figure S7f). Meanwhile, when $Ni(acac)_2$ was changed to $NiCl_2 \cdot 6H_2O$, hcp IrNi NBs were also obtained, but with a shorter nanobranch (Figure S8a–e). The EDS spectrum shows that the Ir/Ni atomic ratio is 10.2/89.8 (Figure S8f).

In order to gain a comprehensive understanding of the formation mechanism of hcp IrNi NBs, a series of control experiments were performed. Firstly, the function of oleylamine (OAm) was investigated by changing OAm to octadecene (ODE), octadecylamine (ODA) and hexadecylamine (HDA). As shown in Figures S9a, b and S10a, when ODE served as the solvent, IrNi nanodendrites with Ir/Ni atomic ratio of 61.8/38.2 were prepared. No characteristic peaks attributed to hcp phase can be found from the XRD pattern (Figure S11). When ODA and HDA were used to replace OAm, IrNi nanobranches formed, with the Ir atomic percentages as low as 11.8% and 24.9%, respectively (Figures S9c, e and S10b, c). Moreover, their hcp phase was identified by the corresponding SAED and XRD patterns (Figures S9d, f and S11). These results indicate that the formation of hcp phase may be related to the final atomic ratio of Ir/Ni in this reaction system. The amino group in OAm, ODA and HDA can coordinate strongly with Ir^{3+} (Figure S12), and reduce the reduction tendency of Ir^{3+}, resulting in low atomic ratio of Ir/Ni.[50–53] Secondly, the role of oleic acid (OA) was investigated as well. When OA was changed to heptanol and ethylene glycol, only irregular

nanoparticles were formed (Figure S13a,c). Though the branched structures can be obtained by replacing OA with benzyl alcohol, the uniformity of products is very poor (Figure S13b). Notably, only nanoparticles with hcp phase can be obtained without adding OA (Figures S14a,b and S15). With increasing the amount of OA from 0.2 to 1 mL, the multi-rod-like nanobranches were well maintained with a little change of the Ir/Ni atomic ratio (Figures S14c,e,g,i and S16), and their crystal phase is always hcp (Figures S14d,f,h,j and S15). These results indicate that OA acts as a structure directing reagent, which is crucial for the formation of branched structures. As reported, in hcp phase metal nanostructures, the surface energy of $(002)_h$ is lower than those of $(010)_h$, $(101)_h$ and $(110)_h$ due to the high coordination number of surface atoms.[54–57] Thus the growth direction should occur on high-surface-energy facets theoretically. Nonetheless, in our reaction system, the anisotropic growth of nanobranches is along the $[001]_h$ direction instead. This may be attributed to the selective adsorption of OA and/or OAm on the side facets of nanobranches.[36,58–63] Thirdly, it was found that formaldehyde plays a bifunctional role for the formation of well-defined nanobranches and unconventional hcp phase (Figure S17). In the absence of formaldehyde, fcc nanoparticles (NPs) were formed (Figures S18a,b and S19). With adding 50 μL of formaldehyde solution, branched nanostructures with the co-existence of fcc and hcp phases were obtained (Figures S18c,d and S19). When 100 μL of formaldehyde solution were added, well-defined IrNi nanobranches with pure hcp phase were successfully synthesized (Figures S18e,f and S19). However, the hcp phase nanobranch structures turned to be large nanoparticles by further increasing the amount of formaldehyde solution to 400 μL (Figures S18g–l and S19). These results suggest that the presence of formaldehyde is significantly essential to the formation of hcp phase, and its dosage will largely affect the morphology of products. Besides, the atomic ratio of Ir decreases from 25.6 % to 6.3 %, with increasing the amount of formaldehyde solution from 0 to 400 μL (Figure S20). During the solvothermal process, with elevating the reaction temperature, the formaldehyde can be decomposed into CO and H_2.[64–66] The produced H_2 and OAm in the reaction system could promote the preferential reduction of Ni^{2+} ions, although the standard reduction potential of Ni^{2+}/Ni (−0.25 V vs standard hydrogen electrode (SHE)) is more negative than that of Ir^{3+}/Ir (1.16 V vs SHE).[50–51,58,61] As more H_2 was produced with increasing the dosage of formaldehyde solution, the atomic ratio of Ir became lower. In the absence of $Ni(acac)_2$, the yield of products was very little (Figure S21). That would be attributed to the strong coordination abilities of the amino and carboxylic acid functional groups in OAm and OA to Ir^{3+}, which significantly reduce the reduction potential of Ir^{3+}/Ir and slow down the reduction rate of Ir^{3+}. On the other hand, without adding $Ir(acac)_3$, irregular Ni nanoparticles will be formed (Figure S22). These results suggest that the co-reduction of Ir and Ni is prerequisite for hcp IrNi NBs. Therefore, the effects of the feeding atomic ratio of Ni/Ir on the formation of well-defined hcp IrNi NBs were further explored. As shown in Figures S23a,b and S24, when the feeding atomic ratio of Ni:Ir is 1:2, irregular nanoparticles with fcc phase were obtained. The ultimate Ir atomic percentage is 49.2 % (Figure S25a). With increasing the atomic ratio from 1:1 to 10:1, the Ir contents of products gradually decrease but with pure hcp phase (Figures S23d,f,h,j,i, S24 and S25b–f). But only when the feeding atomic ratios are 2:1 and 3:1, the well-defined nanobranch structures can be obtained (Figure S23e,g). The corresponding atomic ratios of Ir/Ni are 20.5/79.5 and 12.5/87.5, respectively (Figure S25c,d). These results indicate that the feeding atomic ratio of metal precursors is of great significance for the synthesis of hcp IrNi alloy nanobranches.

For the hcp IrNi NBs, the HAADF-STEM and EDS line scanning results have revealed a Ni-rich core and Ir-rich shell structure (Figure 1 and Figure S6). This could originate from the preferential reduction of Ni rather than Ir due to the syngenetic effects of OAm, OA and the produced H_2.[51] The trace oxygen in the reaction solution may also contribute to etching the low-coordinated Ni and facilitate the formation of such structure.[67–68] On the other hand, it has been reported that CO could induce the diffusion of Pt atoms from the inner core to surface sites.[36,69] In our reaction system, Ir may also diffuse to the shell part owing to the presence of CO generated by the decomposition of formaldehyde. Furthermore, time-dependent experiments were conducted to study the formation mechanism of hcp IrNi NBs. No products were obtained after 1 h reaction. When the reaction time was 2 h, Ni-rich polyhedron-shape nanoparticles as well as some branched structures with Ir/Ni atomic ratio of 15.7/84.3 were formed (Figure S26a–c). The fcc structure was determined by the XRD pattern (Figure S27). As the reaction continued, nanobranches formed at the reaction time of 4 h (Figure S26d,e), which may derive from the polymorphism of Ni.[59] The atomic ratio of Ir/Ni shows a slight decrease to 10.4/89.6 (Figure S26f). The XRD pattern identifies the co-existence of common fcc phase and unconventional hcp phase (Figure S27). Considering that the $(111)_f$ facet of fcc phase has an identical close-packed arrangement of atoms to that of $(002)_h$ facet of hcp phase, it is reasonable to propose that the hcp phase nanobranches should originate from the fcc Ni-rich nanoparticles formed at 2 h. As the reaction proceeded to 6 h, the morphology of samples is similar to that obtained at 4 h (Figure S26g,h). The atomic ratio of Ir/Ni is 14.5/85.5 (Figure S26i). The XRD pattern shows pure hcp phase (Figure S27). When the reaction time reached 8 h and 11 h, the morphology of products shows a little change, and the pure hcp phase is still maintained (Figures S26j,k,m,n and S27). The Ir/Ni atomic ratios increase from 16.3/83.7 to 20.0/80.0 (Figure S26l,o). Finally, after 14 h reaction, well-defined hcp IrNi NBs with Ir/Ni atomic ratio of 20.5/79.5 was obtained (Figure 1, and Figures S1, S3 and S5). Based on the abovementioned control experiments and time-dependent results, a possible mechanism for the synthesis of hcp IrNi NBs has been proposed. Firstly, Ir^{3+} and Ni^{2+} were reduced into Ni-rich fcc IrNi nanoparticles with polyhedron-shape. Then the Ni-rich IrNi nanobranches gradually grew along the $[111]_f$ direction and evolved into pure hcp

structure along the $[001]_h$ direction due to the syngenetic effects of OAM, OA and formaldehyde. With further increasing the reaction time, the Galvanic replacement reaction between Ni-rich nanobranches and Ir precursor occurred on the surface of Ni-rich IrNi nanobranches. Meanwhile, Ni^{2+} and Ir^{3+} in solution were reduced and selectively deposited along the $[001]_h$ direction. At last, unconventional hcp phase IrNi nanobranches with a Ni-rich core and Ir-rich shell were successfully obtained.

By using the same method, IrRhNi alloy NBs with unconventional hcp phase have also been prepared. TEM and HAADF-STEM images show that the obtained IrRhNi NBs are assembled by multiple rodlike nanobranches with a core-shell structure (Figure S28a and Figure 2a, b). The

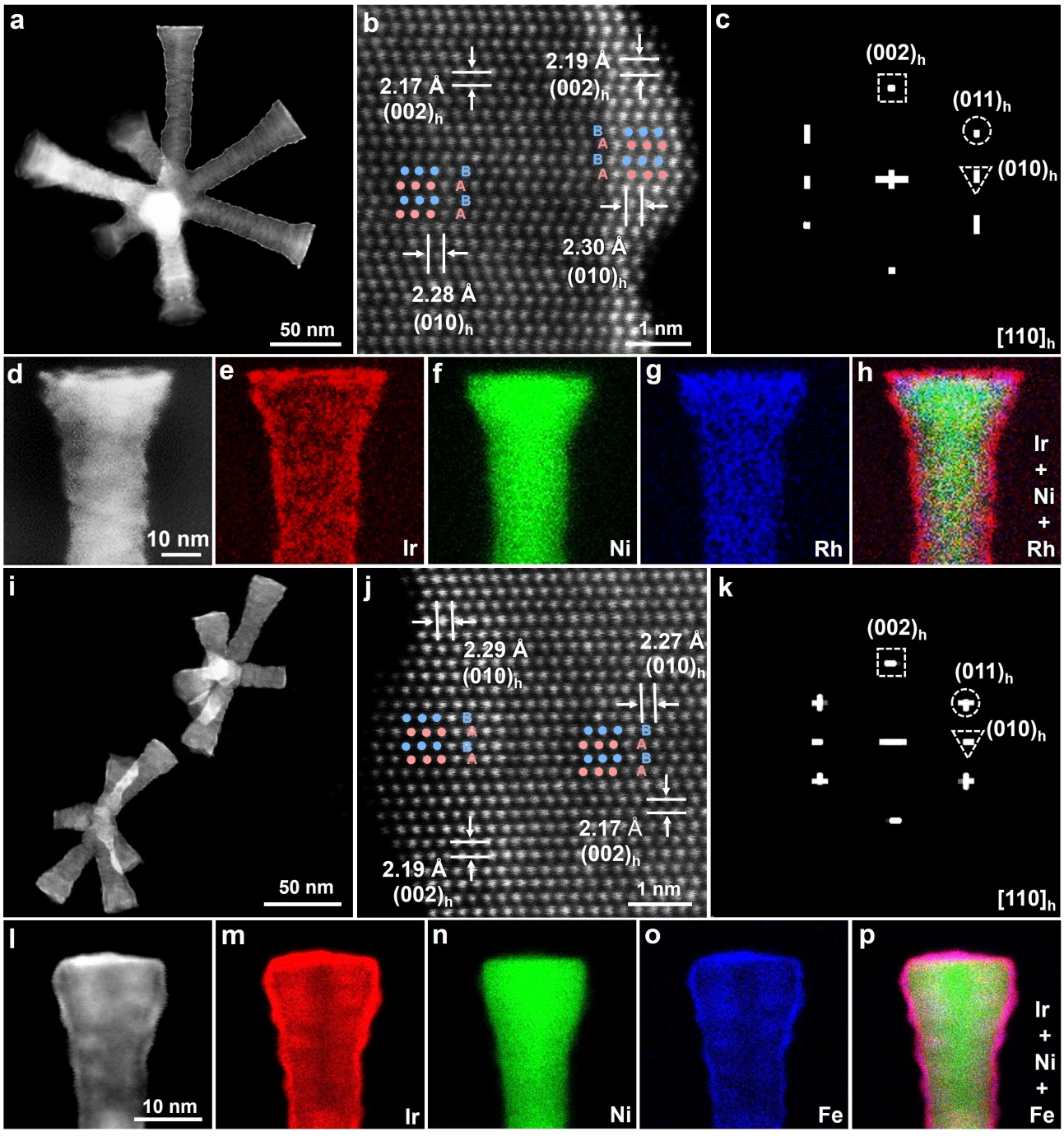

Figure 2. Structural characterization of unconventional hcp phase IrRhNi and IrFeNi alloy NBs. (a, b) HAADF-STEM image (a) and atomic-resolution HAADF-STEM image (b) of hcp IrRhNi NBs. (c) The corresponding FFT pattern generated from (b). (d–h) The HAADF-STEM image (d) and the corresponding EDS elemental mappings (e–h) of individual hcp IrRhNi NBs. (i, j) HAADF-STEM image (i) and atomic-resolution HAADF-STEM image (j) of hcp IrFeNi NBs. (k) The corresponding FFT pattern generated from (j). (l–p) The HAADF-STEM image (l) and the corresponding EDS elemental mappings (m–p) of individual hcp IrFeNi NBs.

SAED pattern of IrRhNi NBs can be assigned to the hcp phase, which is also determined by the XRD pattern (Figures S28b and S29). The characteristic stacking sequence of "AB" along the close-packed $[001]_h$ direction of hcp phase can be clearly observed at both the core and shell regions. The measured lattice spacings of 2.17 (2.19) and 2.28 (2.30) Å are assigned to $(002)_h$ and $(010)_h$ facets of hcp phase at the core (shell) sites, respectively (Figure 2b). The corresponding FFT pattern matches well with the diffraction pattern of hcp phase along the $[110]_h$ zone axis (Figure 2c). The XPS spectra confirm the dominant metallic states of Ir, Rh, and Ni in hcp IrRhNi NBs (Figure S30). The EDS spectrum demonstrate that the atomic ratio of Ir/Rh/Ni is 12.5/78.3/9.2 (Figure S31). Moreover, the alloy structure with Ni-rich core and Ir-rich shell for the obtained hcp IrRhNi NBs was identified by the EDS line scanning and elemental mapping results (Figure S32 and Figure 2d–h).

In addition, the unconventional hcp phase IrFeNi alloy NBs can also be prepared by replacing the metal precursor of $Rh(acac)_3$ with $Fe(acac)_3$. TEM and HAADF-STEM images exhibit that the obtained IrFeNi nanostructures possess a similar morphology with IrNi and IrRhNi NBs (Figure S33a and Figure 2i). The hcp phase of IrFeNi NBs was confirmed by both SAED and XRD patterns (Figures S33b and S34). Moreover, at both the core and shell sites, the atomic-resolution HAADF-STEM images clearly show the characteristic atomic arrangement of hcp phase (Figure 2j). The measured lattice spacings of 2.17 (2.19) and 2.27 (2.29) Å are ascribed to $(002)_h$ and $(010)_h$ facets of hcp phase at the core (shell) sites, respectively. The corresponding FFT pattern can also be well assigned to the hcp phase along the $[110]_h$ zone axis (Figure 2k). The main metallic states of Ir, Fe, and Ni within IrFeNi NBs were identified by XPS spectra (Figure S35). The EDS spectrum demonstrates that the atomic ratio of Ir/Fe/Ni is 17.5/71.1/11.4 (Figure S36). In addition, the EDS line scanning and elemental mapping characterizations reveal the alloys structure of hcp IrFeNi NBs, which also possess a Ir-rich shell and Ni-rich core (Figure S37 and Figure 2l–p).

X-Ray Spectral Analysis

Besides unconventional hcp phase IrNi alloy NBs, the common fcc phase IrNi alloy NPs with a similar atomic ratio of Ir/Ni to hcp IrNi NBs were also prepared (Figures S38–S40). X-ray photoelectron spectroscopy (XPS) was used to investigate the electronic structures of hcp IrNi NBs and fcc IrNi NPs. As shown in Figure S41, Ir mainly exists in the metallic state with a slight oxidation of surface atoms in both hcp IrNi NBs and fcc IrNi NPs. Compared to fcc IrNi NPs, the Ir 4f peak positions of hcp IrNi NBs show a negative shift by about 0.20 eV, indicating the higher electron density of Ir and stronger interaction between Ir and Ni.[70–71] The Ni 2p XPS spectra of both samples suggest that the dominant valance of Ni is metallic state, which should benefit from the IrNi alloy structure (Figure S42).

X-ray absorption spectroscopy (XAS) was further utilized to study the electronic structures and local coordination environments of as-synthesized hcp IrNi NBs and fcc IrNi NPs. In the Ir L_3-edge X-ray absorption near-edge structure (XANES) spectra, the white line intensities of hcp IrNi NBs and fcc IrNi NPs are close to that of Ir powder, but far below that of IrO_2, suggesting that Ir mainly adopts the metallic state but with a slight oxidation (Figure 3a). Figure 3b shows the k^2-whighted Fourier-transform Ir L_3-edge extended X-ray absorption fine structure (EXAFS) spectra. There is one dominant peak located at around 2.51 Å for Ir powder, which is assigned to the Ir–Ir scattering path. While the dominant peaks at about 2.27 Å for hcp IrNi NBs and fcc IrNi NPs are ascribed to the Ir–Ir or Ir–Ni scattering paths. The shorter Ir–Ir or Ir–Ni bond lengths in hcp IrNi NBs and fcc IrNi NPs than that in the pure Ir powder is attributed to the formation of IrNi alloy nanostructures. Besides, no obvious Ir–O scattering paths can be observed, which further indicates the main metallic states of Ir in both hcp IrNi NBs and fcc IrNi NPs. The fitting results show that hcp IrNi NBs and fcc IrNi NPs have the same bond lengths of Ir–Ir and Ir–Ni (Table S1 and Figure S43a–c). The coordination numbers (C.N.) of Ir–Ir and Ir–Ni in hcp IrNi NBs are 5.8 and 4.9, respectively, which are similar to those in fcc IrNi NPs, suggesting the substantial alloying of Ir with Ni. These results collaborate that Ir demonstrates a similar coordination environment in hcp IrNi NBs and fcc IrNi NPs.

In the Ni K-edge XANES spectra, the white line intensities of hcp IrNi NBs and fcc IrNi NPs are slightly higher than that of Ni foil but much lower than that of NiO, indicating the main metallic state of Ni in both samples (Figure 3c). As shown in the k^2-weighted Ni K-edge EXAFS spectra, no obvious Ni–O scattering paths appear in these two samples, and the position of the dominant peak in fcc IrNi NPs and hcp IrNi NBs is close to that in Ni foil, suggesting the dominant metallic state of Ni in both nanostructures (Figure 3d). The fitting results show that the C.N. of Ni–Ni is much higher than that of Ni–Ir in fcc IrNi NPs and hcp IrNi NBs, which means that a small amount of Ni coordinates with Ir to form the IrNi alloy structure (Table S2 and Figure S43d–f). These results agree well with the observation of the unique structure with Ni-rich core and Ir-rich shell by the TEM and EDS. But the larger C.N. of Ni–Ir in hcp IrNi NBs over fcc IrNi NPs suggests the higher alloy degree of Ni in hcp IrNi NBs. Meanwhile, the larger bond length of Ni–Ni in hcp IrNi NBs (2.58 Å) than those in Ni foil with fcc phase (2.48 Å) and fcc IrNi NPs (2.51 Å) elucidates the successful formation of hcp structure.[58] The intensity maxima of wavelet transforms (WTs) of Ir L_3-edge EXAFS spectra of fcc IrNi NPs and hcp IrNi NBs are similar with each other, and show downward shift than Ir powder, suggesting the formation of the IrNi alloy structure (Figure 3e). In the Ni K-edge WT, the intensity maxima of fcc IrNi NPs and hcp IrNi NBs are close to that of Ni foil, which further identifies the metallic state of Ni (Figure 3f).

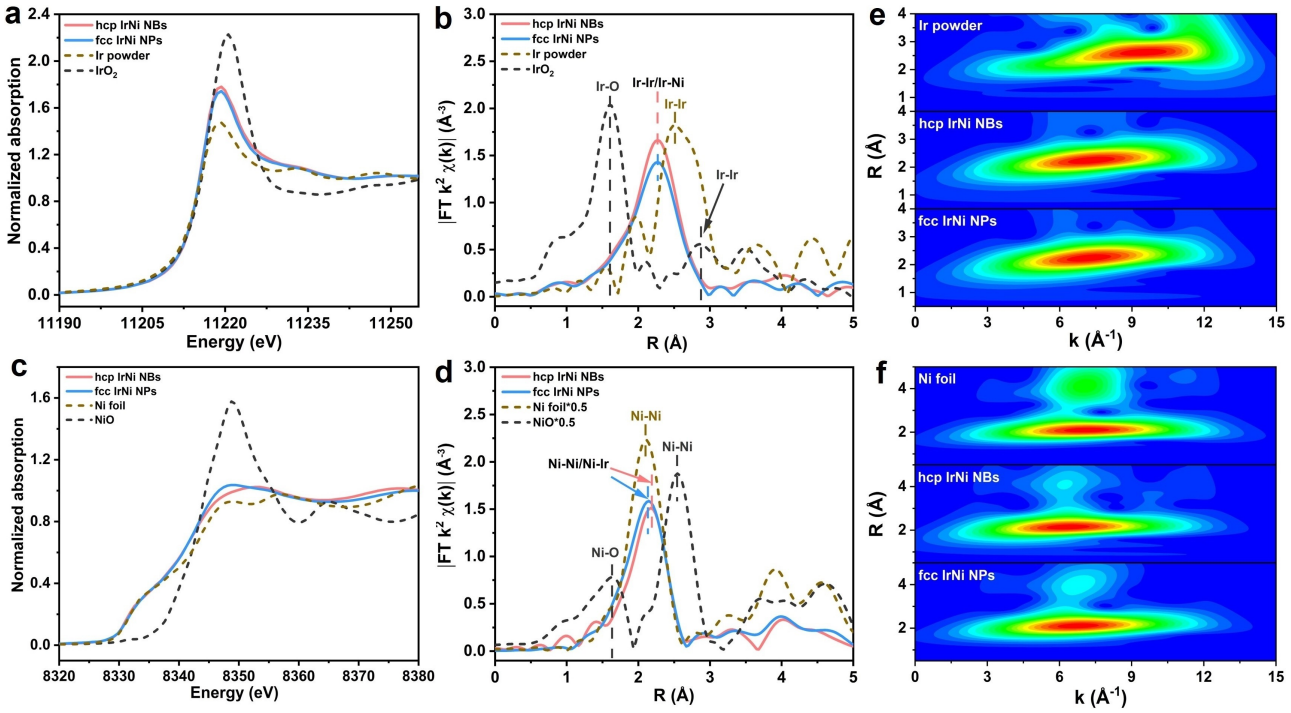

Figure 3. X-ray spectral analysis. (a, b) Normalized Ir L_3-edge XANES (a) and Fourier transform k^2-weighted EXAFS (b) spectra of hcp IrNi NBs, fcc IrNi NPs, Ir powder, and IrO_2. (c, d) Normalized Ni K-edge XANES (c) and Fourier transform k^2-weighted EXAFS (d) spectra of hcp IrNi NBs, fcc IrNi NPs, Ni foil, and NiO. (e) Wavelet transforms of Ir L_3-edge EXAFS spectra of Ir powder, hcp IrNi NBs and fcc IrNi NPs. (f) Wavelet transforms of Ni K-edge EXAFS spectra of Ni foil, hcp IrNi NBs and fcc IrNi NPs.

Electrochemical NO_2RR Performance

As a proof-of-concept application, the as-prepared unconventional hcp IrNi alloy NBs and fcc IrNi alloy NPs were utilized as catalysts in electrocatalytic NO_2RR. The electrocatalytic performance was tested in a standard H-type cell by using the electrolyte containing 1 M KOH and 0.1 M KNO_2. As shown in Figure 4a, in the presence of KNO_2, hcp IrNi NBs deliver a much higher current density, suggesting their better NO_2RR performance over fcc IrNi NPs. Chronoamperometry measurements with the potential range of 0.3 to −0.1 V (vs RHE) were further conducted to evaluate the NO_2RR performance of hcp IrNi NBs and fcc IrNi NPs (Figures S44 and S45). Significantly, the hcp IrNi NBs demonstrate the highest NH_3 FE of 98.2 % at 0 V (vs RHE), which is much larger than fcc IrNi NPs (87.2 %). Notably, the NH_3 FE of hcp IrNi NBs can be well maintained above 90 % at a wide potential range from 0.1 to −0.05 V (vs RHE) (Figure 4b). Meanwhile, hcp IrNi NBs also demonstrate a much higher NH_3 yield rate, and achieve the highest value of 34.6 $mg\,h^{-1}\,mg_{cat}^{-1}$ (or 75.5 $mg\,h^{-1}\,mg_{Ir}^{-1}$) at −0.1 V (vs RHE), which is 1.97 (1.84) times that of fcc IrNi NPs (17.6 $mg\,h^{-1}\,mg_{cat}^{-1}$ (or 41.0 $mg\,h^{-1}\,mg_{Ir}^{-1}$)) (Figure 4c). Correspondingly, hcp IrNi NBs exhibit a superior partial current density of NH_3 over that of fcc IrNi NPs, and reach the maximum value of 49.9 $mA\,cm^{-2}$ at −0.1 V (vs RHE) (Figure S46). After normalized by electrochemical active surface area (ECSA), the NH_3 yield rate of hcp IrNi NBs is much larger than that of fcc IrNi NPs, suggesting their superior intrinsic activity in NO_2RR (Figures S47 and S48). In addition, hcp IrNi NBs can also achieve a much higher energy efficiency (EE) in the whole potential range, with the highest value of 50.1 % at 0.1 V (vs RHE) (Figure 4d). It should be highlighted that hcp IrNi NBs exhibit outstanding NH_3 FE, EE and yield rate at low overpotentials, surpassing most of the reported catalysts for NO_2RR (Table S3). Besides NH_3, the potential byproducts, including hydrazine (N_2H_4) and H_2, were also detected by ultraviolet-visible (UV/Vis) spectroscopy and gas chromatography, respectively. As the applied potential became more negative to −0.1 V (vs RHE), the FE of N_2H_4 gradually decreased to 0.5 %, while that of H_2 increased to 11.5 % (Figure S49). At 0 V (vs RHE), the amount of N_2H_4 and H_2 is negligible, which confirms the high selectivity to NH_3 synthesis.

Considering the practical application of nitrite contamination removal, the influence of nitrite concentration on NO_2RR was further explored. Impressively, the superior catalytic performance of hcp IrNi NBs can be well maintained over a wide range of nitrite concentrations. In specific, with decreasing the NO_2^- concentration from 0.1 M to 0.01 M, the highest NH_3 FE and EE only show a little decrease from 98.2 % to 93.3 % and from 50.1 % to 47.3 %, respectively (Figure 4e and Figure S50). Meanwhile, the highest NH_3 yield rate of 10.1 $mg\,h^{-1}\,mg_{cat}^{-1}$ can still be achieved with 0.01 M NO_2^-, demonstrating the promising potential for NH_3 production with practical wastewater. Note that when the nitrite concentration increases to 0.2 M,

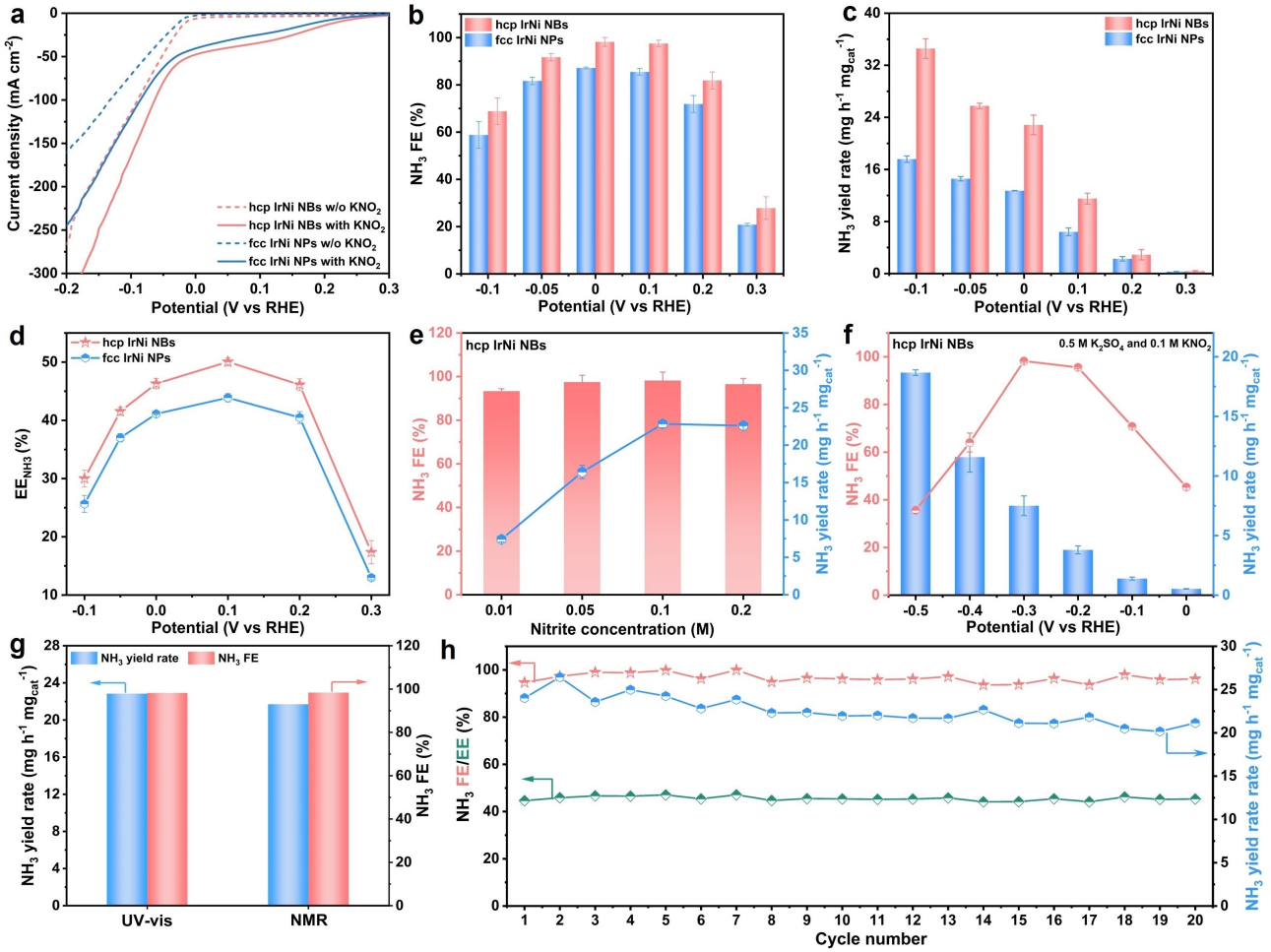

Figure 4. Electrocatalytic NO_2RR performance. (a) LSV curves of hcp IrNi NBs and fcc IrNi NPs in 1 M KOH with and without (w/o) 0.1 M KNO_2. (b–d) NH_3 FE (b), yield rate (c), and half-cell energy efficiency (EE) (d) of hcp IrNi NBs and fcc IrNi NPs at various potentials. (e) NH_3 FE and yield rate of hcp IrNi NBs at 0 V (vs RHE) with different nitrite concentrations. (f) The NH_3 FE and yield rate of hcp IrNi NBs in the neutral electrolyte composed of 0.5 M K_2SO_4 and 0.1 M KNO_2 at different potentials. (g) The NH_3 FE and yield rate of hcp IrNi NBs at 0 V (vs RHE) by UV/Vis and NMR methods. (h) The consecutive recycling electrolysis test of hcp IrNi NBs at 0 V (vs RHE) toward NO_2RR.

the NH_3 FE, EE, and yield rate show a slight decrease compared to those of 0.1 M, which may be attributed to the insufficient active hydrogen supply. Besides, the electrochemical NO_2RR performance at different hydroxyl concentrations was also investigated (Figure S51). It was observed that the hydroxyl concentration exerts insignificant effect on NH_3 production. In particular, hcp IrNi NBs still exhibit the highest NH_3 FE, EE and yield rate of 96.8 %, 48.4 % and 21.1 $mg\,h^{-1}mg_{cat}^{-1}$, respectively, when the hydroxyl concentration is as low as 0.1 M. Moreover, in the neutral condition, hcp IrNi NBs can achieve the highest NH_3 FE of 98.6 % at −0.3 V (vs RHE) as well as the largest NH_3 yield rate of 18.7 $mg\,h^{-1}mg_{cat}^{-1}$ at −0.5 V (vs RHE) (Figure 4f and Figure S52). It was found that the pH of electrolyte changed to 11.71 and 12.38 after electrolysis at −0.3 and −0.5 V (vs RHE), respectively (Figure S53). The NO_2RR performance of hcp IrNi NBs in neutral-buffered solution was further performed. As shown in Figure S54, hcp IrNi NBs can achieve the highest NH_3 FE of 96.3 % and the largest NH_3 yield rate of 21.8 $mg\,h^{-1}mg_{cat}^{-1}$ at −0.1 and −0.5 V (vs RHE), respectively, and it only showed a slight change of pH after electrolysis compared with the initial state (Figure S55). These results reveal the great potential of hcp IrNi NBs as highly efficient catalysts for NH_3 production in NO_2RR under practical conditions.

Besides, control experiments were conducted with bare carbon paper and hcp IrNi NBs as the electrodes to confirm the origin of nitrogen source as well as the accuracy of NO_2RR performance measurement. As expected, negligible NH_3 can be detected on bare carbon paper in the absence or presence of KNO_2 (Figure S56). In contrast, the current density and NH_3 yield rate of hcp IrNi NBs are negligible without KNO_2, but increase a lot after introducing KNO_2. Moreover, as shown in the NMR spectrum, no peaks attributed to NH_4^+ can be observed without adding KNO_2 in the electrolyte (Figure S57). Importantly, the NH_3 FE and yield rate calculated by ultraviolet-visible (UV/Vis) approach are well consistent with those obtained by the NMR method (Figure 4g and Figure S58). Furthermore, it has been confirmed that the NH_3 volatilization in the electro-

lytes (pH 14) is negligible during the 1 h electrolysis (Figure S59), suggesting the good accuracy and high reliability of the electrochemical results.

The catalytic stability of hcp IrNi NBs in NO_2RR was evaluated by the consecutive recycling electrolysis at 0 V (vs RHE). During the 20 consecutive electrolysis cycles, the NH_3 FE and yield rate kept stable, suggesting the superior catalytic durability of hcp IrNi NBs toward NO_2RR (Figure S60 and Figure 4h). Notably, after the stability test, the morphology, composition, and crystal phase of hcp IrNi NBs can be well preserved, which is verified by the TEM, selected-area electron diffraction (SAED), and EDS characterizations (Figure S61a–c). Moreover, the core-shell structure composed by Ni-rich core and Ir-rich shell can be well maintained, which was verified by the EDS elemental mappings and line scanning profiles (Figure S61d–h). All the above results confirm the superior catalytic stability of unconventional hcp phase IrNi alloy NBs in electrocatalytic NO_2RR.

Mechanism Investigation

It was found that hcp IrNi NBs demonstrate a much smaller Tafel slope (131 mV dec^{-1}) than that of fcc IrNi NPs (172 mV dec^{-1}), suggesting the efficient electron transfer efficiency and rapid reaction kinetics of hcp IrNi NBs in NO_2RR (Figure S62).[15,72] During the electrochemical process of NO_2RR, the subsequent conversion of NO_2* is significantly influenced by the formation and consumption rate of active hydrogen (H*).[21–22] As shown in Figure S47, the corresponding H* area of hcp IrNi NBs is 20.7 % larger than that of fcc IrNi NPs, suggesting that hcp IrNi NBs are capable of providing more H* for the conversion of NO_2^- to NH_3.[73] To directly confirm the existence of H*, EPR test was performed by using 5,5-dimethyl-1-pyrroline N-oxide (DMPO) as the H* trapping reagent.[74–76] During electrolysis without KNO_2, hcp IrNi NBs exhibit a much stronger DMPO-H signal compared to fcc IrNi NPs, which suggests that hcp IrNi NBs have a superior ability for the H* generation (Figure 5a). Upon the addition of KNO_2, the signal intensity of fcc IrNi NPs only displays a slight decrease, while a significant reduction of the DMPO-H signal intensity can be observed on hcp IrNi NBs (Figure 5b). This result indicates that the H* generated on hcp IrNi NBs can be rapidly consumed, ensuring the swift conversion of nitrogen-containing intermediates into NH_3. Moreover, a certain amount of tert-butyl alcohol (TBA) was introduced into the electrolyte to effectively trap the generated H*.[77–78] As the concentration of TBA increases, there is an obvious decrease in both current density and NH_3 yield rate, indicating the critical role of the equilibrium between H* formation and consumption in NH_3 synthesis (Figure S63 and Figure 5c).

In situ DEMS characterization was further performed to gain a comprehensive understanding of the reaction process of NO_2RR.[15,79–80] Throughout the five cycles of linear sweep voltammetry (LSV) scanning, the mass/charge (m/z) signals of 2, 14, 15, 16, 17, 28, 30, 31, 33, and 46 attributed to H_2, N, NH, NH_2, NH_3, N_2, NO, HNO, NH_2OH, and NO_2, respectively, were detected for both hcp IrNi NBs and fcc IrNi NPs (Figure 5d,e and Figure S64). The reaction pathway of NO_2RR could follow: NO_2*→NO*→NOH* (HNO*)→NHOH* (N*)→NH_2OH* (NH*)→NH_2*→NH_3*→NH_3. Moreover, The hcp IrNi NBs demonstrate a lower overpotential for the formation of several nitrogen-containing intermediates and the ultimate product, i.e., NH_2OH, NO, HNO, N, NH, NH_2, and NH_3 (Figure 5f,g and Figure S64a–e). Meanwhile, the much higher H_2 peak intensity of hcp IrNi NBs than that of fcc IrNi NPs reveals their stronger ability to generate sufficient H* for the hydrogenation of nitrogen-containing intermediates (Figure S64f). These observations uncover that the unconventional hcp phase IrNi alloy NBs possess superior catalytic activity for the formation of H* and the subsequent hydrogenation of nitrogen-containing intermediates toward NH_3 production.

Theoretical Calculations

DFT calculations were further performed to investigate the distinct electronic structures and reaction trends for hcp IrNi NBs and fcc IrNi NPs towards the NO_2RR. The surface electronic distributions near the Fermi level (E_F) have been demonstrated for comparisons on both hcp and fcc IrNi alloys (Figure 6a,b). It is noted that the bonding orbitals show much stronger contributions on the hcp IrNi surface than the fcc IrNi surface, indicating that the hcp surface is more electroactive. After geometry relaxation, the hcp surface exhibits more evident lattice distortion near the Ir sites, which is potentially attributed to the strong interactions between the Ir-rich shell and the Ni-rich core. Notably, such surface distorted regions have contributed to the bonding orbitals of the surface, leading to significant modulations of surface activity. Accordingly, the electron transfer efficiency and adsorptions of the key intermediates on the hcp surface are improved to support the fast NO_2RR kinetics. In addition, by comparing different Ir : Ni ratios in the shell structures, it is noted that the formation energy costs increase as Ir concentration increases (Figure S65). The optimal balance of the electroactivity and stability is obtained by the similar concentrations of Ir and Ni in the shell. The more in-depth analysis of the electronic structures is further performed through the projected partial density of states (PDOSs) on both hcp and fcc IrNi alloys (Figure 6c,d). For the hcp IrNi NBs, it was noticed that Ni-3d orbitals have dominated the electron density near the E_F with slight splitting. Meanwhile, the Ir-5d orbitals have shown broad coverage, which pins the Ni-3d orbitals in the middle. This guarantees a stable valence state of Ni on the surface during the electrocatalysis. The e_g-t_{2g} splitting in Ir-5d orbitals is nearly absent, revealing the small energy barriers of electron transfer on the surface of hcp IrNi NBs. In contrast, for the fcc IrNi NPs, the Ni-3d orbitals remain similar while the e_g-t_{2g} splitting becomes more evident with a barrier of 0.98 eV, resulting in reduced electron transfer efficiency. The d-band center of Ir has also been slightly

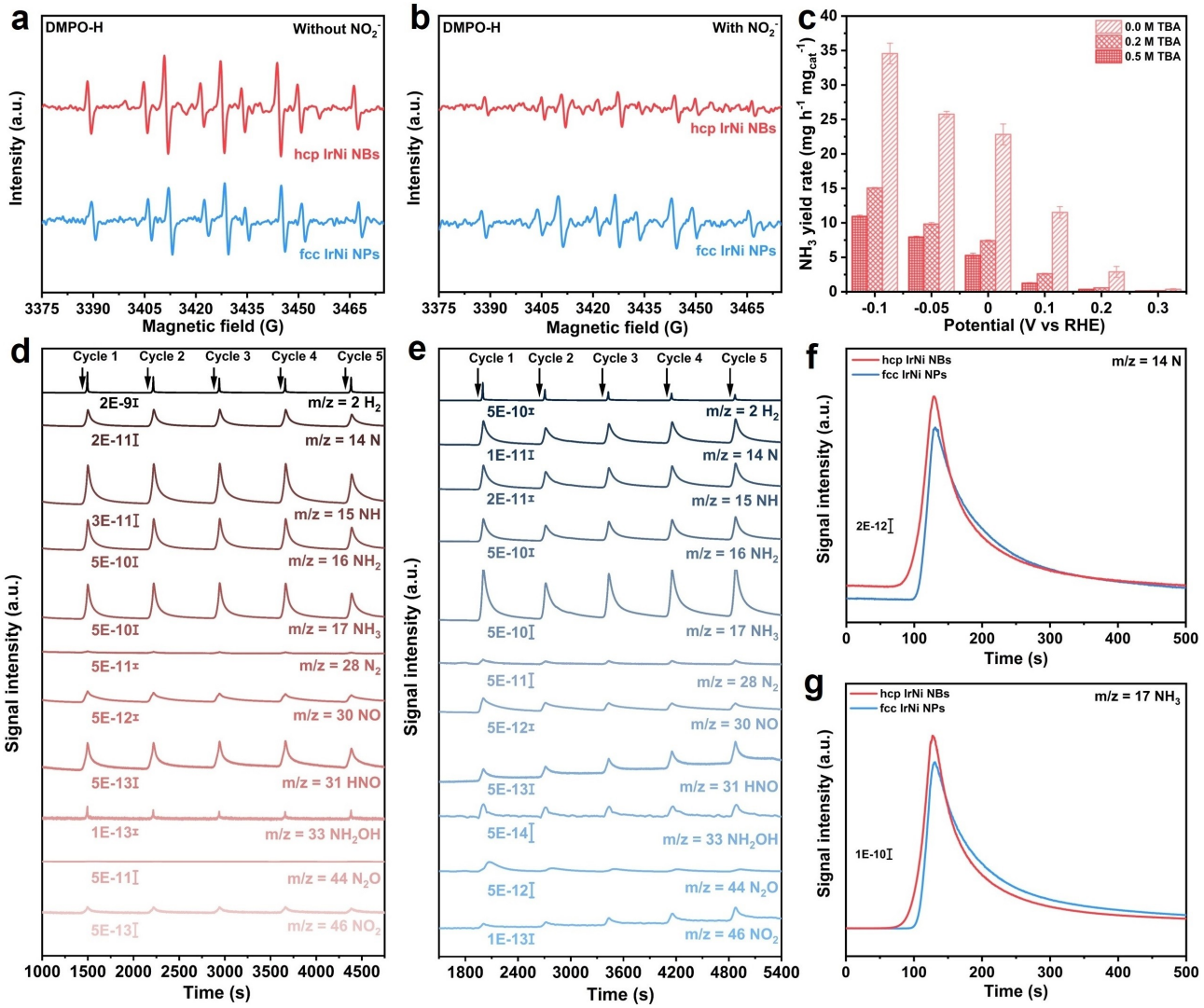

Figure 5. Mechanism investigation of NO_2RR. (a, b) DMPO-involved EPR spectra of hcp IrNi NBs and fcc IrNi NPs without (a) and with (b) NO_2^-. (c) NH_3 yield rates of hcp IrNi NBs in the potential range from 0.3 to −0.1 V (vs RHE) without and with different TBA concentrations. (d, e) In situ DEMS patterns of hcp IrNi NBs (d) and fcc IrNi NPs (e) for NO_2RR. (f, g) In situ DEMS patterns for the detection of N* (f) and NH_3 (g) on hcp IrNi NBs and fcc IrNi NPs.

downshifted from $E_V-1.80$ eV ($E_V=0$ eV) on the hcp IrNi alloy to $E_V-1.86$ eV on the fcc IrNi alloy. This reveals a slightly higher valence state of Ir sites in the hcp phase, which are more electroactive to accomplish electron transfer with the intermediates and promote the NO_2RR. Moreover, the site-dependent PDOSs of Ir in hcp and fcc IrNi are compared to unravel the distinct electronic structures (Figure 6e). For Ir-5d orbitals, the e_g-t_{2g} splitting is evident in both bulk Ir metal and the fcc phase of IrNi alloy. However, in the hcp IrNi alloy, the e_g-t_{2g} splitting has been significantly alleviated, especially for the shell part of the core-shell structure. From the core-shell interface to the shell surface, the barrier of the e_g-t_{2g} splitting largely decreases with increased electron density near E_F, supporting the highly efficient electron transfer behaviors. These are attributed to two strong interactions including the core-shell interaction and the Ir–Ni interaction. For the Ni-3d orbitals, both hcp and fcc phases display similar electronic structures to the bulk Ni metal, demonstrating that Ni sites are close to the metallic state (Figure 6f). Compared to the fcc phase and bulk metal, the Ni-3d in the hcp phases are slightly downshifted, which is induced by the stronger interactions between Ni and Ir. The superior electroactivity of the hcp IrNi originates from the stronger electron transfer between Ir and Ni due to the higher alloying level, which optimizes the adsorptions of key intermediates to accelerate the NO_2RR. With the optimized electronic structures, the hcp IrNi surface should deliver distinct adsorption behaviors to the fcc IrNi surface, which is distinguished based on the PDOSs evolutions of key intermediates (Figure 6g,h). From the initial activation of NO_2*, the hcp IrNi shows a good linear relationship to guarantee fast electron transfer for each reaction step. In comparison, it was noticed that the s,p orbitals of adsorbed N* on the fcc IrNi surface exhibit a

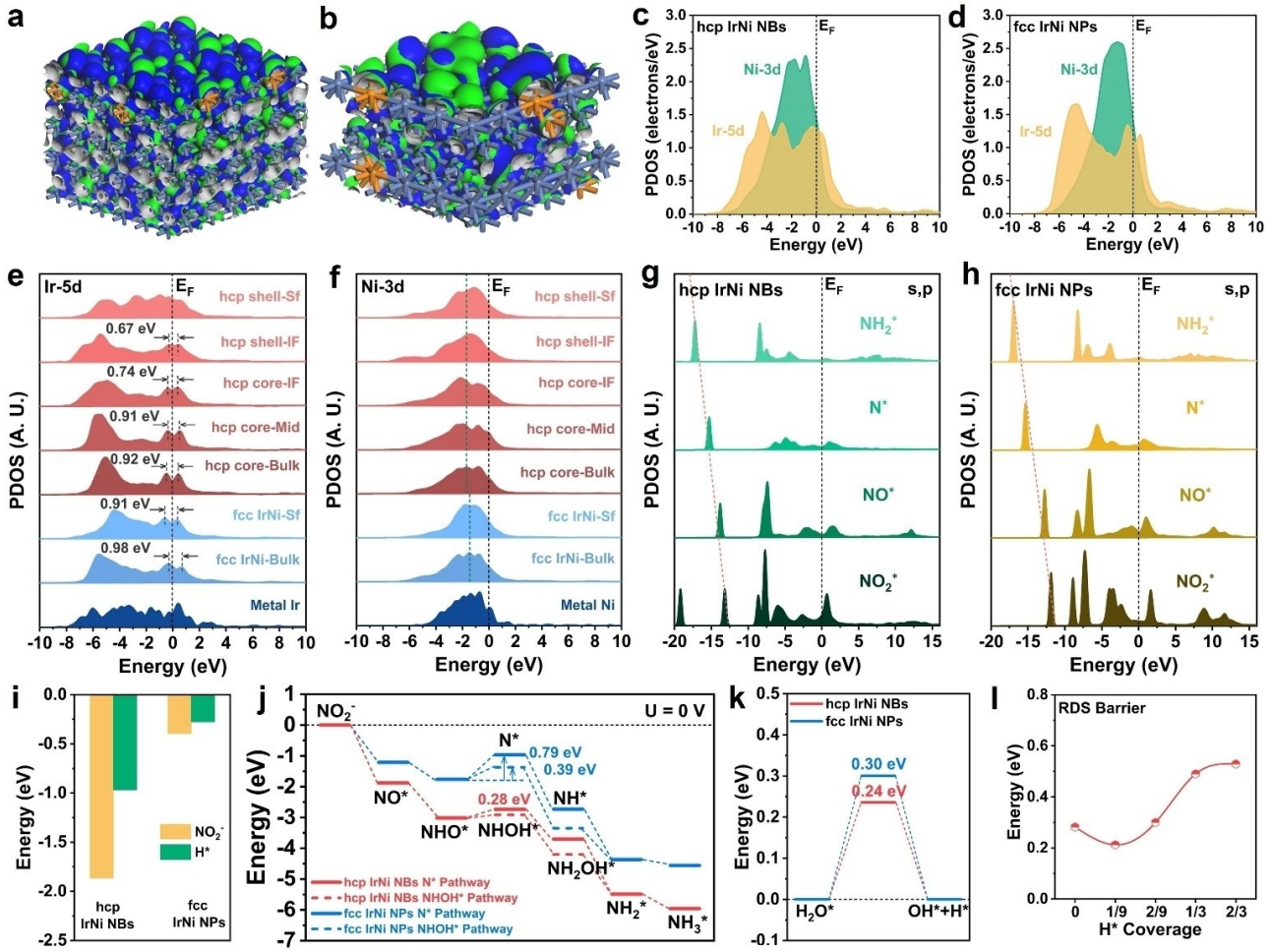

Figure 6. Theoretical calculations of the NO_2RR performance. (a, b) The electronic distributions of bonding and anti-bonding orbitals near the Fermi level (E_F) of hcp IrNi NBs (a) and fcc IrNi NPs (b). Blue balls = Ni and orange balls = Ir. Blue isosurface = bonding orbitals and green isosurface = anti-bonding orbitals. (c, d) The PDOSs of hcp IrNi NBs (c) and fcc IrNi NPs (d). (e, f) Site-dependent PDOSs of Ir-5d (e) and Ni-3d (f) orbitals in hcp IrNi NBs and fcc IrNi NPs. (g, h) The PDOSs evolutions of key intermediates during NO_2RR on hcp IrNi NBs (g) and fcc IrNi NPs (h). (i) The adsorption of key reactants on hcp IrNi NBs and fcc IrNi NPs. (j) The reaction energies of NO_2RR. (k) The water dissociation energy comparison. (l) The energy barrier of RDS with different active hydrogen (H*) coverage.

more evident deviation from the linear relationship, leading to the increased energy barriers during the NO_2RR.

In the meantime, the reaction trends of NO_2RR have also been explored from the energetic aspects. The adsorption energies of both NO_2^- and H* on hcp IrNi NBs are more negative than fcc IrNi NPs, which are critical to quickly activate the NO_2RR process (Figure 6i). Meanwhile, the affinity to NO_2^- on hcp IrNi NBs is much stronger than that of the H*, supporting the suppressed HER. The adsorption configurations are further revealed that NO_2^- prefers to stabilize on the hollow active site, which will be dissociated into NO*, supporting the strong electroactivity of the hcp IrNi alloy (Figure S66). As the reduction processes proceed, the active sites with the most stable adsorption configurations of key intermediates shift from hollow sites to bridge sites and Ni-top sites at the final reaction steps. The fcc IrNi alloy also exhibits a preference for hollow sites (Figure S67). Accordingly, the overall reaction trends of NO_2RR on hcp IrNi NBs are more energetically favored than the fcc IrNi NPs with reduced energy barriers (Figure 6j). For NO_2RR, the main energy barriers on both hcp and fcc phases occur at the reduction of NHO*, where the NHOH* pathway shows lower energy barriers than the N* pathway, indicating the formation of N* is the rate-determining step (RDS). The hcp IrNi displays a much smaller energy barrier (0.28 eV) than that of the fcc IrNi (0.79 eV), resulting in a more efficient NO_2RR process with a higher NH_3 yield rate. The hcp IrNi is able to eliminate all the energy barriers through the NHOH* reaction pathway with an applied potential of −0.10 V, indicating a more efficient NO_2RR than the fcc IrNi under the same potentials (Figure S68).

In addition, the influences of the active hydrogen are also unraveled regarding the energy barrier for the water dissociation (Figure 6k). The hcp IrNi NBs require an energy barrier of 0.24 eV to generate active hydrogen, which is easier than the fcc IrNi NPs with a higher energy barrier of 0.30 eV. Different from the NO_2^-, we notice that H* is

preferred to adsorb on the bridge sites of hcp IrNi, which avoids blocking the surface active sites (Figure S69a). In contrast to the hcp IrNi, the competition between NO_2^- and H* becomes stronger on the similar preference for active sites, which decreases the NO_2RR performances and enhances the competitive HER process (Figure S69b). Moreover, the HER is potentially affected by the evident increasing energy costs when the H* coverage reaches 1/3 (Figure S69c). With the generation of H* on the catalyst surface, the coverage of H* not only induces stronger surface distortions (Figure S69d–f) but also affects the energy barrier of RDS for NO_2RR (Figure 6l). As the H* coverage increases, the RDS barrier on the hcp IrNi NBs decreases from 0.28 eV to the lowest 0.21 eV at the H* coverage of 1/9. As the H* coverage further increases, the RDS barrier evidently increases to 0.48 eV at the 1/3 coverage of H*, which is potentially attributed to the surface distortion, suggesting that the suitable H* coverage is beneficial to improve the NO_2RR performance.

Conclusion

In summary, we have successfully developed a general one-pot solvothermal method for the controlled synthesis of IrNi, IrRhNi and IrFeNi alloy nanobranches with unconventional hcp phase. Interestingly, the obtained hcp IrNi, IrRhNi and IrFeNi NBs possess a unique core-shell alloy structure, with Ni-rich core and Ir-rich shell. As a proof-of-concept application, the representative hcp IrNi alloy NBs demonstrate much superior catalytic performance in NO_2RR compared to the fcc IrNi NPs. Significantly, hcp IrNi NBs exhibit an excellent NH_3 FE of 98.2 % and large EE of 50.1 % at 0 and 0.1 V (vs RHE), respectively. Meanwhile, hcp IrNi NBs can also display an outstanding NH_3 yield rate of 34.6 $mg\,h^{-1}\,mg_{cat}^{-1}$ (75.5 $mg\,h^{-1}\,mg_{Ir}^{-1}$) at −0.1 V (vs RHE). Moreover, hcp IrNi NBs also possess superior catalytic durability during the 20 consecutive electrolysis cycles. In addition, it is worth noting that even at a low nitrite concentration of 0.01 M, an excellent NH_3 FE of 93.3 % can still be achieved at 0 V (vs RHE). Alternatively, in the neutral condition (0.5 M K_2SO_4 and 0.1 KNO_2), hcp IrNi NBs can also show an excellent FE of 98.6 % and a superior yield rate of 18.7 $mg\,h^{-1}\,mg_{cat}^{-1}$ toward NH_3 synthesis. In the neutral-buffered solution composed of 0.5 M PBS (phosphate-buffered solution) and 0.1 KNO_2, hcp IrNi NBs can also deliver excellent NH_3 FE of 96.3 % and yield rate of 21.8 $mg\,h^{-1}\,mg_{cat}^{-1}$ at −0.1 and −0.5 V (vs RHE), respectively. EPR and in situ DEMS studies have revealed that hcp IrNi NBs are capable of generating abundant H* for the hydrogenation of nitrogen-containing intermediates and thus reduce the overpotential for NH_3 production. DFT calculations have indicated that the Ir–Ni interactions not only optimize the electronic structures of the catalyst but also accelerate the electron transfer efficiency on the hcp IrNi alloy NBs. The superior NO_2RR performances are ascribed to the strong Ir–Ni interactions, which largely facilitate the stabilization of key intermediates and the generation of active hydrogen to reduce the reaction barriers. It is believed that this work not only provides a general method to the controlled synthesis of unconventional phase metal nanomaterials, but also offers a feasible strategy for the rational design of advanced NO_2RR electrocatalysts towards a sustainable nitrogen cycle.

Acknowledgements

This work was supported by grants (Project No. 22175148 and 22005258) from National Natural Science Foundation of China, grant (Project No. 21309322; 15304023) from Research Grants Council of Hong Kong, grant (Project No. JCYJ20220530140815035; JCYJ20220531090807017) from Shenzhen Science and Technology Program, ITC via Hong Kong Branch of National Precious Metals Material Engineering Research Centre (NPMM), and grants (Project No. 9610480, 9610663, 9680301 and 7006007) from City University of Hong Kong, National Natural Science Foundation of China/Research Grant Council of Hong Kong Joint Research Scheme (Project No. N_PolyU502/21), National Natural Science Foundation of China/Research Grants Council of Hong Kong Collaborative Research Scheme (Project No. CRS_PolyU504/22), and Natural Science Foundation of Guangdong Province (2023A1515012219). Prof. B. Huang also thank the support from Research Centre for Carbon-Strategic Catalysis (RC-CSC), Research Institute for Smart Energy (RISE), and Research Institute for Intelligent Wearable Systems (RI-IWEAR) of the Hong Kong Polytechnic University.

Conflict of Interest

The authors declare no competing financial interest.

Data Availability Statement

The data that support the findings of this study are available from the corresponding author upon reasonable request.

Keywords: metal nanomaterials · unconventional phase · electrocatalysis · ammonia · nitrogen cycle

[1] D. E. Canfield, A. N. Glazer, P. G. Falkowski, *Science* **2010**, *330*, 192–196.
[2] J. N. Galloway, A. R. Townsend, J. W. Erisman, M. Bekunda, Z. Cai, J. R. Freney, L. A. Martinelli, S. P. Seitzinger, M. A. Sutton, *Science* **2008**, *320*, 889–892.
[3] N. Gruber, J. N. Galloway, *Nature* **2008**, *451*, 293–296.
[4] Y. Xiong, Y. Wang, J. Zhou, F. Liu, F. Hao, Z. Fan, *Adv. Mater.* **2023**, 10.1002/adma.202304021.
[5] X. Zhu, X. Fan, H. Lin, S. Li, Q. Zhai, Y. Jiang, Y. Chen, *Adv. Energy Mater.* **2023**, *13*, 2300669.
[6] J. Liang, B. Deng, Q. Liu, G. Wen, Q. Liu, T. Li, Y. Luo, A. A. Alshehri, K. A. Alzahrani, D. Ma, X. Sun, *Green Chem.* **2021**, *23*, 5487–5493.

[7] S. E. Braley, J. Xie, Y. Losovyj, J. M. Smith, *J. Am. Chem. Soc.* **2021**, *143*, 7203–7208.
[8] X. Zhang, Y. Wang, Y. Wang, Y. Guo, X. Xie, Y. Yu, B. Zhang, *Chem. Commun.* **2022**, *58*, 2777–2787.
[9] F. Wang, H. Zhao, G. Zhang, H. Zhang, X. Han, K. Chu, *Adv. Funct. Mater.* **2023**, 10.1002/adfm.202308072.
[10] R. Hao, L. Tian, C. Wang, L. Wang, Y. Liu, G. Wang, W. Li, G. A. Ozin, *Chem Catal.* **2022**, *2*, 622–638.
[11] S.-L. Meng, C. Zhang, C. Ye, J.-H. Li, S. Zhou, L. Zhu, X.-B. Li, C.-H. Tung, L.-Z. Wu, *Energy Environ. Sci.* **2023**, *16*, 1590–1596.
[12] R. Zhang, S. Zhang, Y. Guo, C. Li, J. Liu, Z. Huang, Y. Zhao, Y. Li, C. Zhi, *Energy Environ. Sci.* **2022**, *15*, 3024–3032.
[13] Y. Wang, M. Sun, J. Zhou, Y. Xiong, Q. Zhang, C. Ye, X. Wang, P. Lu, T. Feng, F. Hao, F. Liu, J. Wang, Y. Ma, J. Yin, S. Chu, L. Gu, B. Huang, Z. Fan, *Proc. Nat. Acad. Sci.* **2023**, *120*, e2306461120.
[14] F. Y. Chen, Z. Y. Wu, S. Gupta, D. J. Rivera, S. V. Lambeets, S. Pecaut, J. Y. T. Kim, P. Zhu, Y. Z. Finfrock, D. M. Meira, G. King, G. Gao, W. Xu, D. A. Cullen, H. Zhou, Y. Han, D. E. Perea, C. L. Muhich, H. Wang, *Nat. Nanotechnol.* **2022**, *17*, 759–767.
[15] S. H. Han, H. J. Li, T. L. Li, F. P. Chen, R. Yang, Y. F. Yu, B. Zhang, *Nat. Catal.* **2023**, *6*, 402–414.
[16] M. Xie, S. Tang, Z. Li, M. Wang, Z. Jin, P. Li, X. Zhan, H. Zhou, G. Yu, *J. Am. Chem. Soc.* **2023**, *145*, 13957–13967.
[17] J. Zhou, Y. Xiong, M. Sun, Z. Xu, Y. Wang, P. Lu, F. Liu, F. Hao, T. Feng, Y. Ma, J. Yin, C. Ye, B. Chen, S. Xi, Y. Zhu, B. Huang, Z. Fan, *Proc. Nat. Acad. Sci.* **2023**, *120*, e2311149120.
[18] G. Wen, J. Liang, Q. Liu, T. Li, X. An, F. Zhang, A. A. Alshehri, K. A. Alzahrani, Y. Luo, Q. Kong, X. Sun, *Nano Res.* **2021**, *15*, 972–977.
[19] Z. Ke, D. He, X. Yan, W. Hu, N. Williams, H. Kang, X. Pan, J. Huang, J. Gu, X. Xiao, *ACS Nano* **2023**, *17*, 3483–3491.
[20] T. Zhu, Q. Chen, P. Liao, W. Duan, S. Liang, Z. Yan, C. Feng, *Small* **2020**, *16*, 2004526.
[21] P. Kunal, C. Yan, H. Guo, H. Li, C. E. Brady, M. Duncan, X. Zhan, C. J. Werth, G. Henkelman, S. M. Humphrey, *ACS Catal.* **2023**, *13*, 11945–11953.
[22] H. Li, C. Yan, H. Guo, K. Shin, S. M. Humphrey, C. J. Werth, G. Henkelman, *ACS Catal.* **2020**, *10*, 7915–7921.
[23] S. Seraj, P. Kunal, H. Li, G. Henkelman, S. M. Humphrey, C. J. Werth, *ACS Catal.* **2017**, *7*, 3268–3276.
[24] C. Wang, W. Zhou, Z. Sun, Y. Wang, B. Zhang, Y. Yu, *J. Mater. Chem. A* **2021**, *9*, 239–243.
[25] D. Zhao, J. Liang, J. Li, L. Zhang, K. Dong, L. Yue, Y. Luo, Y. Ren, Q. Liu, M. S. Hamdy, Q. Li, Q. Kong, X. Sun, *Chem. Commun.* **2022**, *58*, 3669–3672.
[26] R. Wang, Z. Wang, X. Xiang, R. Zhang, X. Shi, X. Sun, *Chem. Commun.* **2018**, *54*, 10340–10342.
[27] Q. Liu, Q. Liu, L. Xie, L. Yue, T. Li, Y. Luo, N. Li, B. Tang, L. Yu, X. Sun, *Chem. Commun.* **2022**, *58*, 5160–5163.
[28] L. Yi, P. Shao, H. Li, M. Zhang, X. Peng, K. Chen, X. Liu, Z. Wen, *J. Power Sources* **2023**, *559*, 232668.
[29] Y. Chen, Z. Lai, X. Zhang, Z. Fan, Q. He, C. Tan, H. Zhang, *Nat. Chem. Rev.* **2020**, *4*, 243–256.
[30] M. Zhao, Y. Xia, *Nat. Rev. Mater.* **2020**, *5*, 440–459.
[31] Z. Fan, H. Zhang, *Acc. Chem. Res.* **2016**, *49*, 2841–2850.
[32] Z. Fan, H. Zhang, *Chem. Soc. Rev.* **2016**, *45*, 63–82.
[33] W. Tong, B. Huang, P. Wang, L. Li, Q. Shao, X. Huang, *Angew. Chem. Int. Ed.* **2020**, *59*, 2649–2653.
[34] S. Lu, J. Liang, H. Long, H. Li, X. Zhou, Z. He, Y. Chen, H. Sun, Z. Fan, H. Zhang, *Acc. Chem. Res.* **2020**, *53*, 2106–2118.
[35] J. Zhou, T. Wang, L. Chen, L. Liao, Y. Wang, S. Xi, B. Chen, T. Lin, Q. Zhang, C. Ye, X. Zhou, Z. Guan, L. Zhai, Z. He, G. Wang, J. Wang, J. Yu, Y. Ma, P. Lu, Y. Xiong, S. Lu, Y. Chen, B. Wang, C. S. Lee, J. Cheng, L. Gu, T. Zhao, Z. Fan, *Proc. Nat. Acad. Sci.* **2022**, *119*, e2204666119.
[36] Z. Cao, Q. Chen, J. Zhang, H. Li, Y. Jiang, S. Shen, G. Fu, B. A. Lu, Z. Xie, L. Zheng, *Nat. Commun.* **2017**, *8*, 15131.
[37] K. Liu, H. Yang, Y. Jiang, Z. Liu, S. Zhang, Z. Zhang, Z. Qiao, Y. Lu, T. Cheng, O. Terasaki, Q. Zhang, C. Gao, *Nat. Commun.* **2023**, *14*, 2424.
[38] Z. Li, X. Wen, F. Chen, Q. Zhang, Q. Zhang, L. Gu, J. Cheng, B. Wu, N. Zheng, *ACS Catal.* **2021**, *11*, 8798–8806.
[39] Z. Fan, M. Bosman, Z. Huang, Y. Chen, C. Ling, L. Wu, Y. A. Akimov, R. Laskowski, B. Chen, P. Ercius, J. Zhang, X. Qi, M. H. Goh, Y. Ge, Z. Zhang, W. Niu, J. Wang, H. Zheng, H. Zhang, *Nat. Commun.* **2020**, *11*, 3293.
[40] Y. Zheng, Y. Jiao, Y. Zhu, L. H. Li, Y. Han, Y. Chen, M. Jaroniec, S. Z. Qiao, *J. Am. Chem. Soc.* **2016**, *138*, 16174–16181.
[41] Y. Wang, F. Hao, M. Sun, M. T. Liu, J. Zhou, Y. Xiong, C. Ye, X. Wang, F. Liu, J. Wang, P. Lu, Y. Ma, J. Yin, H. C. Chen, Q. Zhang, L. Gu, H. M. Chen, B. Huang, Z. Fan, *Adv. Mater.* **2024**, 10.1002/adma.202313548.
[42] Y. Ge, Z. Huang, C. Ling, B. Chen, G. Liu, M. Zhou, J. Liu, X. Zhang, H. Cheng, G. Liu, Y. Du, C.-J. Sun, C. Tan, J. Huang, P. Yin, Z. Fan, Y. Chen, N. Yang, H. Zhang, *J. Am. Chem. Soc.* **2020**, *142*, 18971–18980.
[43] Z. Zhang, G. Liu, X. Cui, Y. Gong, D. Yi, Q. Zhang, C. Zhu, F. Saleem, B. Chen, Z. Lai, Q. Yun, H. Cheng, Z. Huang, Y. Peng, Z. Fan, B. Li, W. Dai, W. Chen, Y. Du, L. Ma, C. J. Sun, I. Hwang, S. Chen, L. Song, F. Ding, L. Gu, Y. Zhu, H. Zhang, *Sci. Adv.* **2021**, *7*, eabd6647.
[44] J. Hao, Z. Zhuang, K. Cao, G. Gao, C. Wang, F. Lai, S. Lu, P. Ma, W. Dong, T. Liu, M. Du, H. Zhu, *Nat. Commun.* **2022**, *13*, 2662.
[45] M. Zhou, C. Li, J. Fang, *Chem. Rev.* **2021**, *121*, 736–795.
[46] Q. Yao, Z. Yu, L. Li, X. Huang, *Chem. Rev.* **2023**, *123*, 9676–9717.
[47] B. Chen, Q. Yun, Y. Ge, L. Li, H. Zhang, *Acc. Chem. Res.* **2023**, *4*, 359–372.
[48] K. D. Gilroy, A. Ruditskiy, H. C. Peng, D. Qin, Y. Xia, *Chem. Rev.* **2016**, *116*, 10414–10472.
[49] F. Liu, Z. Fan, *Chem. Soc. Rev.* **2023**, *52*, 1723–1722.
[50] Z. Niu, Q. Peng, M. Gong, H. Rong, Y. Li, *Angew. Chem. Int. Ed.* **2011**, *50*, 6315–6319.
[51] J. Xu, X. Wang, X. Mao, K. Feng, J. Xu, J. Zhong, L. Wang, N. Han, Y. Li, *Energy Environ. Sci.* **2023**, *16*, 6120–6126.
[52] W. Wang, T. He, X. Yang, Y. Liu, C. Wang, J. Li, A. Xiao, K. Zhang, X. Shi, M. Jin, *Nano Lett.* **2021**, *21*, 3458–3464.
[53] W. Wang, X. Shi, T. He, Z. Zhang, X. Yang, Y. J. Guo, B. Chong, W. M. Zhang, M. Jin, *Nano Lett.* **2022**, *22*, 7028–7033.
[54] J. X. Liu, H. Y. Su, D. P. Sun, B. Y. Zhang, W. X. Li, *J. Am. Chem. Soc.* **2013**, *135*, 16284–16287.
[55] J. Watt, C. Yu, S. L. Chang, S. Cheong, R. D. Tilley, *J. Am. Chem. Soc.* **2013**, *135*, 606–609.
[56] H. Lin, J.-X. Liu, H. Fan, W.-X. Li, *J. Phys. Chem. C* **2020**, *124*, 11005–11014.
[57] J. Ding, Y. Ji, Y. Li, G. Hong, *Nano Lett.* **2021**, *21*, 9381–9387.
[58] Z. Zhang, G. Liu, X. Cui, B. Chen, Y. Zhu, Y. Gong, F. Saleem, S. Xi, Y. Du, A. Borgna, Z. Lai, Q. Zhang, B. Li, Y. Zong, Y. Han, L. Gu, H. Zhang, *Adv. Mater.* **2018**, *30*, 1801741.
[59] A. P. LaGrow, S. Cheong, J. Watt, B. Ingham, M. F. Toney, D. A. Jefferson, R. D. Tilley, *Adv. Mater.* **2013**, *25*, 1552–1556.
[60] A. R. Poerwoprajitno, S. Cheong, L. Gloag, J. J. Gooding, R. D. Tilley, *Acc. Chem. Res.* **2022**, *55*, 1693–1702.
[61] F. Dumestre, B. Chaudret, C. Amiens, M.-C. Fromen, M.-J. Casanove, P. Renaud, P. Zurcher, *Angew. Chem. Int. Ed.* **2002**, *114*, 4462–4465.
[62] R. Malakooti, Y. Takhti, R. Mirzajani, *Chin. J. Chem.* **2011**, *29*, 1119–1123.

[63] Y. Soumare, J. Y. Piquemal, T. Maurer, F. Ott, G. Chaboussant, A. Falqui, G. Viau, *J. Mater. Chem.* **2008**, *18*, 5696–5702.
[64] F. Saleem, Z. Zhang, B. Xu, X. Xu, P. He, X. Wang, *J. Am. Chem. Soc.* **2013**, *135*, 18304–18307.
[65] A. X. Yin, W. C. Liu, J. Ke, W. Zhu, J. Gu, Y. W. Zhang, C. H. Yan, *J. Am. Chem. Soc.* **2012**, *134*, 20479–20489.
[66] F. Saleem, B. Xu, B. Ni, H. Liu, F. Nosheen, H. Li, X. Wang, *Adv. Mater.* **2015**, *27*, 2013–2018.
[67] C. Cui, L. Gan, M. Heggen, S. Rudi, P. Strasser, *Nat. Mater.* **2013**, *12*, 765–771.
[68] Y. Pi, Q. Shao, X. Zhu, X. Huang, *ACS Nano* **2018**, *12*, 7371–7379.
[69] A. Oh, H. Baik, D. S. Choi, J. Y. Cheon, B. Kim, H. Kim, S. J. Kwon, S. H. Joo, Y. Jung, K. Lee, *ACS Nano* **2015**, *9*, 2856–2867.
[70] S. Liu, Z. Hu, Y. Wu, J. Zhang, Y. Zhang, B. Cui, C. Liu, S. Hu, N. Zhao, X. Han, A. Cao, Y. Chen, Y. Deng, W. Hu, *Adv. Mater.* **2020**, *32*, 2006034.
[71] J. Xu, X. Wang, X. Mao, K. Feng, J. Xu, J. Zhong, L. Wang, N. Han, Y. Li, *Energy Environ. Sci.* **2023**, 10.1039/D1033EE02382F.
[72] W. He, S. Chandra, T. Quast, S. Varhade, S. Dieckhofer, J. R. C. Junqueira, H. Gao, S. Seisel, W. Schuhmann, *Adv. Mater.* **2023**, *35*, 2303050.
[73] Y. Wang, P. Zhang, X. Lin, G. Zhang, H. Gao, Q. Wang, Z.-J. Zhao, T. Wang, J. Gong, *Sci. China Chem.* **2023**, *66*, 913–922.
[74] Z. Chang, G. Meng, Y. Chen, C. Chen, S. Han, P. Wu, L. Zhu, H. Tian, F. Kong, M. Wang, X. Cui, J. Shi, *Adv. Mater.* **2023**, *35*, 2304508.
[75] K. Chen, Z. Ma, X. Li, J. Kang, D. Ma, K. Chu, *Adv. Funct. Mater.* **2023**, *33*, 2209890.
[76] W. Yu, J. Yu, M. Huang, Y. Wang, Y. Wang, J. Li, H. Liu, W. Zhou, *Energy Environ. Sci.* **2023**, *16*, 2991–3001.
[77] Y. Wang, H. Li, W. Zhou, X. Zhang, B. Zhang, Y. Yu, *Angew. Chem. Int. Ed.* **2022**, *134*, e202202604.
[78] K. Fan, W. Xie, J. Li, Y. Sun, P. Xu, Y. Tang, Z. Li, M. Shao, *Nat. Commun.* **2022**, *13*, 7958.
[79] S. Zhang, J. Wu, M. Zheng, X. Jin, Z. Shen, Z. Li, Y. Wang, Q. Wang, X. Wang, H. Wei, J. Zhang, P. Wang, S. Zhang, L. Yu, L. Dong, Q. Zhu, H. Zhang, J. Lu, *Nat. Commun.* **2023**, *14*, 3634.
[80] H. Luo, S. Li, Z. Wu, Y. Liu, W. Luo, W. Li, D. Zhang, J. Chen, J. Yang, *Adv. Mater.* **2023**, *35*, 202304695.

Manuscript received: February 8, 2024
Accepted manuscript online: April 22, 2024
Version of record online: May 24, 2024